remote sensing

MDPI

Article

Detection and Description of the Different Ionospheric Disturbances that Appeared during the Solar Eclipse of 21 August 2017

Heng Yang [1,*], Enrique Monte Moreno [1] and Manuel Hernández-Pajares [2,3]

[1] Department of Signal Theory and Communications, TALP, Universitat Politècnica de Catalunya, 08034 Barcelona, Spain; enric.monte@upc.edu
[2] Department of Mathematics, IonSAT, Universitat Politècnica de Catalunya, 08034 Barcelona, Spain; manuel.hernandez@upc.edu
[3] IEEC-CTE-CRAE, Institut d'Estudis Espacials de Catalunya, 08034 Barcelona, Spain
* Correspondence: h.yang@upc.edu

Received: 6 September 2018; Accepted: 26 October 2018; Published: date

Abstract: This work will provide a detailed characterization of the travelling ionospheric disturbances (TIDs) created by the solar eclipse of 21 August 2017, the shadow of which crossed the United States from the Pacific to the Atlantic ocean. The analysis is done by means of the Atomic Decomposition Detector of Traveling Ionospheric Disturbances (ADDTID) algorithm. This method automatically detects and characterizes multiple TIDs from the global navigation satellite system (GNSS) observation. The set of disturbances generated by the eclipse has a richer and more varied behavior than that associated with the shock wave directly produced by cooling effects of the moon shadow. This can be modeled in part as if the umbra and penumbra of the eclipse were moving cylinders that intersects with variable elevation angle a curved surface. This projection gives rise to regions of equal penumbra with shapes similar to ellipses, with different centers and foci. The result of this is reflected in the time evolution of the TID wavelengths produced by the eclipse, which depend on the vertical angle of the sun with the surface of the earth, and also a double bow wave phenomenon, where the bow waves are generated in advance to the umbra. We show that the delay in the appearance of the disturbances with the transit of the eclipse are compatible with the physical explanations, linked to the different origins of the disturbances and the wavelengths. Finally, we detected a consistent pattern, in location and time of disturbances in advance to the penumbra as a set of medium scale TIDs, which could be hypothesized as soliton waves of the bow wave. In all cases, the detected disturbances were checked visually on the detrended vertical total electron content (TEC) maps.

Keywords: Multiple Traveling Ionospheric Disturbances; GNSS receiver network; solar eclipse; bow wave

1. Introduction

The ionosphere is the Earth's upper atmosphere primarily ionized by solar radiation and located at the height of ∼50–1000 km. Solar eclipses provide a unique opportunity to study the ionospheric response to the fast and transitory variation of the solar radiation. The effect of the eclipse is the generation of disturbances with different characteristics and behaviour, caused by the interaction of the heat balance in the shaded regions at different heights. The perturbations can be attributed to different phenomena, which have been described theoretically and experimentally in many studies. Typically, the ionospheric response to the eclipse can be studied by means of various observations techniques, such as the incoherent scatter radar [1], ionosonde measurement [2], global navigation

satellite system (GNSS) ionospheric sounding [3] among others. Salah et al. [1] and Le et al. [4] observe the consistently remarkable depletion of the electron density in F region as a direct consequence of the decreased ionizing radiation in the ionosphere. Chimonas and Hines [5] point out that gravity waves generated in middle neutral atmosphere by the eclipse-induced radiative cooling, should build up a bow wave propagating up to E-F region of ionosphere and forming TIDs when the moon's shadow sweeps at supersonic speed. Furthermore, Chimonas [6], Fritts and Luo [7] and Eckermann et al. [8] model and analyze the occurrence, structure and characteristics of the bow wave of atmospheric gravity waves. Davis and Da Rosa [9], Cheng et al. [10] and Zerefos et al. [11] observe the wavelike ionospheric disturbances of atmospheric gravity waves at the D-F1 region during the solar occultation by the moon, but show weak and ambiguous correlations with the bow wave characteristics due to the difficult observation conditions and the existence of other factors that have a greater influence, such as geomagnetic activity, regular solar terminator, etc. In particular, the large dense ground-based GNSS observation network can be used as global ionospheric sensor network to detect and characterize the time-varying and space-varying electron density fluctuations of the ionosphere. The GNSS observation network in particular can be used to measure the disturbances in the ionosphere generated by the transit of the moon's shadow. Liu et al. [12] presented the observations of bow and stern waves in the ionosphere induced by the solar eclipse of 22 July 2009, nevertheless the observations were to a certain extend incomplete because the GNSS network only partially covered the affected region.

In the case of the 2017 solar eclipse, which crossed the United States, the contribution of this work is to provide a detailed characterization of the ionosphere's response to the eclipse's transit. This is due to the fact that in the eclipse passed through an area densely covered by the GNSS observation singular network in the United States. As previous works, we can mention for example, Hernández-Pajares et al. [13] where the authors show the footprint of total electron content (TEC) decrease in the global TEC map during the eclipse, and in Coster et al. [3] the authors note a consistent and significant TEC depletion above US and also the presence of large scale travelling ionospheric disturbances in detail during eclipse transit. In Zhang et al. [14] the authors show three different patterns of eclipse-induced ionospheric perturbations and their approximate characteristics such as the bow-shaped TEC depletion along the totality, the clear behavior of ionospheric bow waves of atmospheric gravity waves and large scale ionospheric waves. In Nayak and Yiğit [15] the authors show two kinds of travelling ionospheric disturbances of atmospheric gravity waves in different intensities, the stronger ones occurring along the totality and the other in the region with lower eclipse magnitude. Finally in Sun et al. [16] the authors describe the occurrence and characteristics of the large scale V-shaped wavefront as a shock wave in F region of the ionosphere. These observations done by means of a dense GNSS network are consistent with the TEC variation prediction by Huba and Drob [17], the simulation of atmosphere-ionosphere response (see McInerney et al. [18] and Wu et al. [19]) and the ionosphere observations by other techniques such as Reinisch et al. [20] and Bullett and Mabie [21]. This indicates the ability of ground-based dense GNSS networks to accurately detect eclipse-induced disturbances.

In the above mentioned literature, most of the authors analyze the disturbances created by the eclipse based on maps by means of visual inspection. In contrast, in this work we will use an algorithm that automatically detects TIDs from a large number of measurements from a GNSS network. These measures include observable fluctuations along the lines at all heights of the ionosphere. Also the bow-shaped gravitational waves. In particular, in this work, we will compare each of the estimated disturbances by means of the Atomic Decomposition Detector of Traveling Ionospheric Disturbances (ADDTID) algorithm with a visual representations of the maps where the associated phenomenon is observed.

In summary, the contribution of this work will be the temporal characterization of the ionospheric disturbances associated with the eclipse of 21 August 2017, by means of an algorithm capable of quickly detecting the temporal variation of the characteristics of multiple simultaneous TIDs. For this, we have used the ADDTID algorithm (see details of the theoretical background and implementation

in Yang et al. [22]), which detects several simultaneous TIDs and yields the changes in wavelength, azimuth and velocity of each wave as a time series.

2. Observation Data and Space Weather

In order to describe the effects of the eclipse on the ionosphere above the United States, we used data from GNSS receivers. The source of the GNSS data is provided by the Continuously Operating Reference Stations (CORS) network of the National Geodetic Survey (NGS). This network consists of almost 2000 ground-based continuous GNSS stations densely distributed in the United States [23] (see Figure 1).

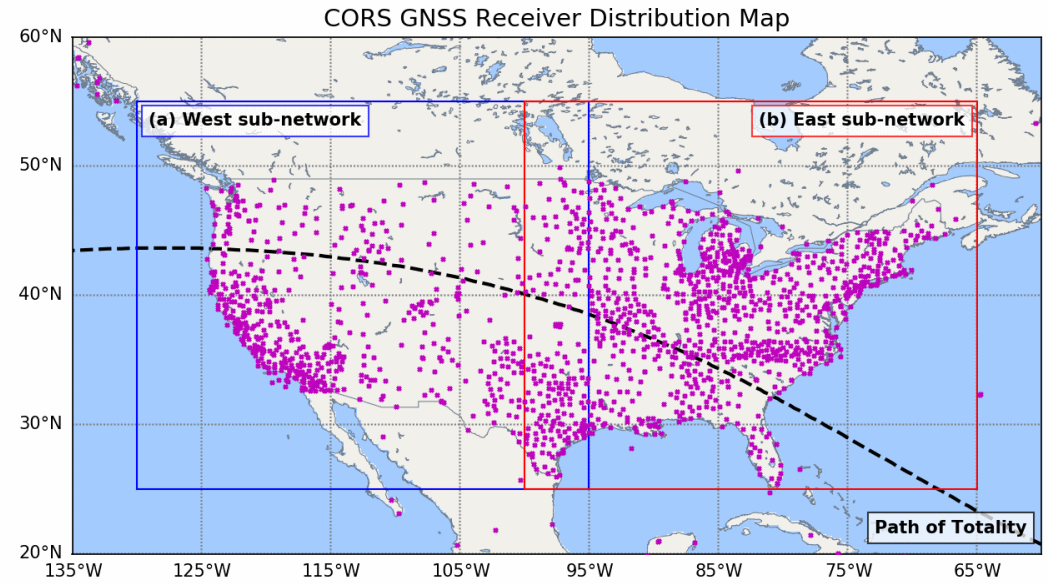

Figure 1. GNSS receivers distribution of CORS in United States and the path of totality for the solar eclipse in August 2017. Magenta dots denote the location of the GNSS receivers, the black dashed line the path of totality, the blue rectangular frame the West sub-network of CORS and the red the East sub-network.

During the duration of the eclipse, the geomagnetic activity was very weak (the planetary 3-hour-range indices $kp \leq 3$, see US Department of Commerce, National Oceanic and Atmospheric Administration (NOAA) [24]), and the auroral electrojet activity was moderate (the AE index $\leq$500 nT, see World Data Center for Geomagnetism, Kyoto [25]). Also there were no significant disturbances originated by natural hazard phenomena such as solar flares, significant earthquakes or tsunamis, that is, no corresponding ionospheric disturbances in the CORS-observing region recorded in [26–28].

3. Methodology

In the introduction, we presented a summary of the possible explanations of the different types of disturbances produced by the eclipse transit over the continent. These include bow waves and other related disturbances. These bow waves consist of several simultaneous TIDs induced by different causes, among them, the upward atmospheric gravity waves [5]. In addition we detected early perturbations, and perturbations that persist after the transit.

In this study, the detection of several simultaneous TIDs was implemented in three steps: (a) The GNSS data preprocessing, that obtains the ionospheric combination from the dual frequency carrier phase data, and computes the detrended TEC data (Section 3.1); (b) the TIDs characterization by means of the ADDTID algorithm that automatically detects them and estimates their parameters (Section 3.2); (c) The details of subdivision criterion of the network for improving the performance of the ADDTID algorithm (Section 3.3).

3.1. GNSS Preprocessing and Detrending

The preprocessing of GNSS data was done as follows: first we obtained the ionospheric combination (also called geometry-free combination) $L_I(t)$ from the dual frequency carrier phases $L_1(t)$ and $L_2(t)$, as the difference $L_I(t) = L_1(t) - L_2(t)$ (in length units). The $L_I(t)$ is an affine function of the slant total electron content (STEC), which we will denote as $S(t)$. This affine function consists of a linear coefficient and an intercept, which takes into account the carrier phase ambiguity and wind-up term. The main components of $S(t)$ are the TEC trends such as diurnal variations and elevation angle variation with low frequency and high energy, which we will denote as background component. Besides, another component of $S(t)$ of interest that has different frequency properties are the ionospheric fluctuations, such as the TIDs.

A method for separating the TID component from the background component, consists of computing the double difference (i.e., bandpass filter) of the time-series of measured $L_I(t)$. We will denote this double difference as $\tilde{S}(t)$ (see Hernández-Pajares et al. [29]). Taking into account the almost constant intercept in $L_I(t)$ when no new losses of lock (cycle slips) occur, we group the time series $L_I(t)$ into independent sub-series defined by the cycle-slips. In each sub-series, the intercepts can be considered constant, and thus can be eliminated by the double time difference divided by -2, that is,

$$\tilde{S}(t) \approx L_I(t) - \frac{1}{2}[L_I(t + \Delta t) + L_I(t - \Delta t)] \quad (1)$$

where Δt is the detrending time interval, which determines the enhanced frequency bands of the TIDs in $\tilde{S}(t)$. Although there is no definite agreement about the characteristics of bow waves generated by the eclipse (see the previous studies Chimonas and Hines [5], Zhang et al. [14] and Nayak and Yiğit [15]), these studies suggest a periodicity of TIDs of 20–60 min. Therefore, we selected $\Delta t = 600$ s for the band pass filter in order to emphasize the eclipse-induced TIDs and also to greatly limit the effect of typical medium scale TIDs with 10 min of periods (see Hernández-Pajares et al. [30]). This value allows high sensibility to the TIDs with periods of 12–60 min. Attenuating the waves by a factor lower than $1/2$ the waves of periods less than 12 min or greater than 60 min, being relatively flat in this band.

The time evolution of the TIDs at different elevation angles is estimated from the detrended VTEC $\tilde{V}(t)$ which in turn is the projection of the detrended STEC $\tilde{S}(t)$ by means of a mapping function $M(t)$, i.e., $\tilde{V}(t) = \frac{\tilde{S}(t)}{M(t)}$, see Hernández-Pajares et al. [31]. This method assumes that $\tilde{S}(t)$ occurs at the ionospheric pierce points (IPPs). These IPPs are located on a shell with the mean effective height corresponding to the height where we assume that the TIDs commonly occur. We discarded observations with an elevation angle of less than 15° as a compromise between obtaining enough TIDs information and the effect of the angle on the mapping function errors.

We took 250 km as the mean effective height to detect these ionospheric disturbances. This is justified by the following reasons: (a) Hernández-Pajares et al. [29] point out that the maximum MSTID generation occurs at the height below hmF2 because the MSTIDs are generated by the interaction between the neutral and ion particles. (b) In the case of this eclipse, Huba and Drob [17] predict the electron density would decrease in E-F region between 150 and 350 km. (c) Nayak and Yiğit [15] and Zhang et al. [14] point out that during the eclipse the height where the ionosphere shows the maximum perturbation typically in the E-F1 region below hmF2, as the response to the atmospheric gravity waves induced by the solar eclipse. (d) Zhang et al. [14] and Sun et al. [16] show the eclipse-induced large scale TIDs should be generated at the F region. (e) The regular hourly height distribution of peak electron density (hmF2) on this day ranged from 240 km to 310 km (obtained from National Aeronautics and Space Administration/Goddard Space Flight Center (NASA/GSFC) [32], see the International Reference Ionosphere 2012 model [33]).

In addition, the TID detection was performed independently for each GPS satellite, because TID activity measured from the detrended VTEC maps could occur at different heights. In addition, the analysis was performed taking this aspect into account.

3.2. Summary of the Atomic Decomposition Detector of Traveling Ionospheric Disturbances Algorithm

The analysis of the data was done by means of the Atomic Decomposition Detector of Traveling Ionospheric Disturbances algorithm (ADDTID, see details in Yang et al. [22]). This algorithm uses data from a dense GNSS receiver network, and can detect and characterize TIDs from the ionospheric piercing points (IPPs). The algorithm creates a dictionary of possible waves that encompass the geographical area under study. The estimation is done using only the IPP samples, and solving a convex optimization problem with a regularization term. This algorithm determines the TIDs as the elements of the dictionary that best approximate the observations at the IPPs. Stating the problem in this way has several advantages, mainly, that the number of possible waves to be detected does not have to be stated beforehand. Also, and perhaps the most challenging aspect of the estimation problem, the algorithm can work with non uniform spatial sampling, including the presence of directions with higher density of sensors, or regions of the network lacking sensors.

In this article (following the presentation in Yang et al. [22]), we have used a dictionary of plane waves. The model of the waves that gives rise to the elements of the dictionary have the following form,

$$A\left(x,y,t\right) = A_0 \cos\left(\vec{k}\cdot\left(x,y\right) - \omega(t-t_0) + \varphi_0\right) \tag{2}$$

where $\vec{k}$ is the 2D angular wave number vector, with the module $\left|\vec{k}\right| = \frac{2\pi}{\lambda}$; λ is the wavelength and the normal vector $\frac{\vec{k}}{|\vec{k}|} = (\cos\theta, \sin\theta)$ points in the direction of propagation of the wave. The wave amplitude is A_0. The terms ω, t_0 and φ_0 are the angular frequency, the starting epoch and initial phase of the TID wave, respectively. The corresponding ith dictionary element $T_i(x,y)$ at epoch t is defined as follows:

$$T_i\left(x,y\right) = \cos\left(\frac{2\pi}{\lambda_i}\left(x\cos\theta_i + y\sin\theta_i\right) + \varphi_i\right) \tag{3}$$

The element $T_i(x,y)$ of the dictionary is characterized by: λ_i wavelength, φ_i phase, and θ_i wave azimuth. The parameters of each element of the dictionary (θ, λ, and φ), are quantized as real numbers, with values restricted to realistic ranges.

The dictionary D is constructed by the concatenation of the set of N elements $T_i(x,y)$, reshaped as vectors, giving an array D, defined as $D = [T_1, T_2, T_3, ..., T_N]$. The elements $T_i(x,y)$ are generated by assigning to the parameters $\{\lambda, \theta, \varphi\}$, all possible feasible values in a quantified range. Each element $T_i(x,y)$ consists of a grid of P_v rows and P_h columns, i.e., a uniform sampling of the geographical region of interest. Then, the array is reshaped to a vector T_i of dimension $P_v \times P_h$. Please note that the observations correspond to the IPPs; hence, in the estimation of the vector, α_t will be done only with the coordinates (x,y) corresponding to measured IPPs. Therefore given a dictionary D, we estimate a set of coefficients at time t, which we denote as α_t, such that the observation V, is approximated by the product $V \approx D\alpha_t$. The observation vector V, is defined by the values observed at the IPPs of each satellite. In order not to change the notation, from now on the dictionary matrix D, is defined so that for each element of the dictionary we only extract the components at the observed IPPs.

The parameter vector α_t, is estimated by means of a trade-off between a loss function (i.e., how well we approximate the observations by means of the model) and a regularization term (i.e., constraints on the possible solutions). The regularization term is used in order to guarantee that the solution should be sparse, that is, only a small set of elements of the dictionary will contribute to the approximation. An estimation technique that allows for the trade-off with a sparse set of coefficients is the LASSO (see for instance Hastie et al. [34]), where the norm on the loss function is ℓ_2, and the norm on the regularization term is ℓ_1. Thus the optimization problem to be solved is,

$$\alpha_t^\star = \arg\min_{\alpha_t} \frac{1}{2}\|V - D\alpha_t\|_{\ell_2} + \rho\|\alpha_t\|_{\ell_1} \tag{4}$$

The parameter ρ controls the level of sparsity of the solution, and is determined automatically from the data, as explained at Yang et al. [22].

3.3. Justification of the Network Subdivision Criterion to Enhance the Performance of the ADDTID Algorithm

The model ADDTID, assumes that the TIDs propagate in the form of plane waves. In practice, the TIDs, as is shown in the Figure 6a, show a propagation pattern that follow the shape of the eclipse isopenumbra lines (shown in white). These isopenumbra lines for different elevations show a shape similar to an ellipse. In this case the equivalent to the eccentricity of an ellipse, depends on the inclination of the eclipse's shadow. These ellipse-shaped shadow gradually decreases the amount of solar irradiance incident on the atmosphere. For the physical intuition of the inclinations and obscurations see Figure 2. This gradual obscuration in space and time, causes the electron density oscillations, that follow a complex and complicated response at different scales. An example of the wealth of phenomena is shown in Figure 6a, which shows the disturbances follow the isopenumbra lines for different inclinations. The disturbances include: bow-shaped wavefronts, partial circular wavefronts, receding ripples and planar wavefronts in different scales. As a precedent, in which similar phenomena are observed see Zhang et al. [14] and Sun et al. [16]. This suggests that a natural model for the dictionary matrix D of the ADDTID algorithm, should include all possible quadratic patterns of wave propagation. Nevertheless this is prohibitive from the computational point of view because the size of the dictionary grows by a polynomial of the number of parameters.

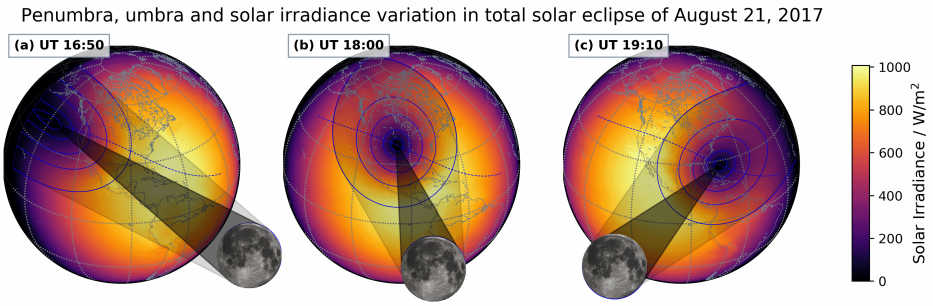

Figure 2. Variations of penumbra, umbra and solar irradiance at three moments of the eclipse, blue solid-line circles denote the penumbra in 25%, 50%, 75%, 90% of obscurations and the umbra, blue dashed line represents the eclipse totality, the color map shows the global horizontal irradiance at the height of 250 km.

As mentioned in Section 3.2, the ADDTID algorithm can approximately estimate these circular waves as compositions of local planar waves. This means, for instance, that a given wave front of a bow wave, would be detected as two planar waves propagating in symmetric directions at each side of the main direction of propagation. In Figure 5, we show a visual example of the validity of the plane wave approximation. In this figure, the detrended VTEC maps over the local net of California show a near plane wave structure, which corresponds to the detected waves at the scatter plot (Figure 5b,c). This scatter plot at 17:15–17:45 UT, shows that the detected planar TIDs are distributed along two main directions that are symmetric with the main propagation azimuth that is approximately 90 degrees. At simple glance, we can see on the map measured at the same moment, there are two flat fronts, with the same azimuths detected by the algorithm. (Note in the subplots at Figure 5e–h, the alignment of dots of same intensity distributed following lines).

This indicates that the size of the measuring network has to be such that the curvature of the wavefront should be small. As is shown in Figure 1, we divided the CORS GNSS network that covers the US into several smaller subnetworks, each covering an area where the resulting TIDs can be locally approximated by a planar wave. The partition into subnetworks was done taking into account the different scale bow waves reported in Zhang et al. [14] and Sun et al. [16], the scheme of division is

two sub-networks, the West Coast and the East Coast. This is because the ADDTID algorithm that was used for detecting the TIDs assumes that the waves to be detected are planar and cover a significant part of the stations. This hypothesis is approximately true if the whole net is partitioned into subnets. A feature of the algorithm that is relevant for this study, is that the estimation is robust to non uniform sampling and the geographical orientation of the set of stations.

In a more detailed way, the division of the network is justified because of the following reasons. (a) The disturbances that are generated by the eclipse can be approximated locally as plane waves, but at the scale of the whole network the curvature can be significant (see for instance Figure 6). Thus, the size of the partition of the network was such that inside a partition the wave front can be approximated as planar, and corresponding parts away from the umbra, which exhibit a greater curvature, are included in the neighbouring partition. (b) As can be seen in Figure 1, the central part of the network has a lower density of stations, which has an effect in the accuracy of the estimation. Therefore it is a natural region for deciding the border between partitions. (c) We allowed for an overlap of about 10% between subnetworks, in order to be able to check the consistency of the estimates between them. (d) Finally, the partition is also justified because the disturbances caused by the eclipse were different from one geographical area to another.

An additional benefit is the fact that the propagation of the waves at either coast follow similar azimuths and wavelengths, but the velocities may sometimes have a different sign. As an example of this see the TID maps in Figures 3d and 4d, where the wavefronts in the west and east parts have differences in their azimuth and wavelength. Another benefit of the geographical partition into sub-nets is that this allows for explaining phenomena that are qualitatively different and might appear mixed if the analysis were done with the entire network.

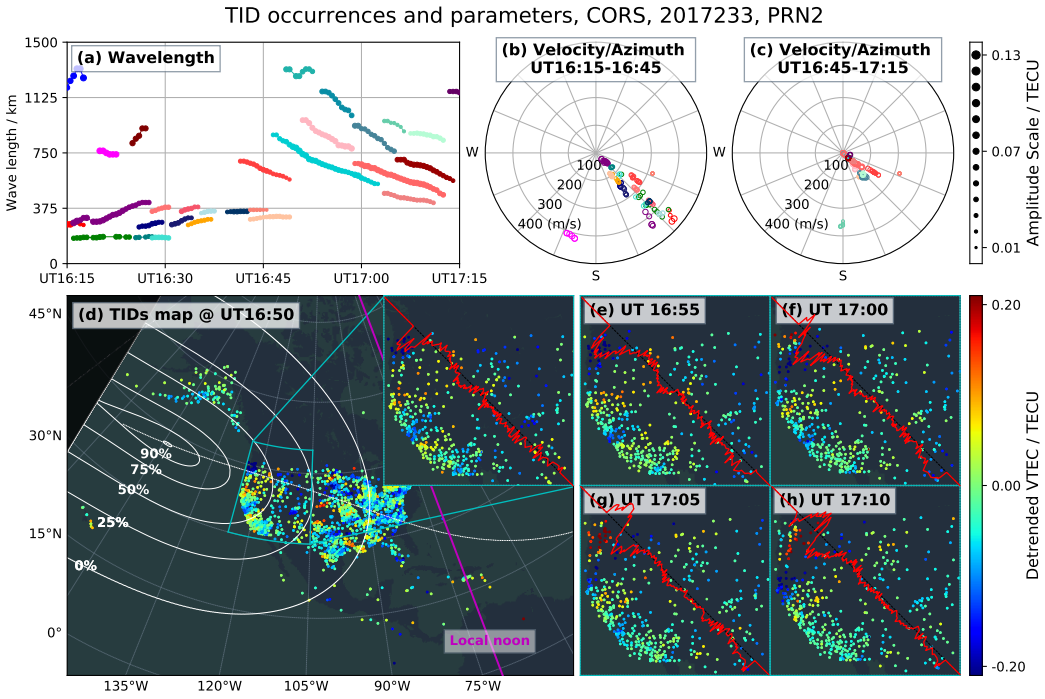

Figure 3. Time-variation plots of the TIDs parameters, when the penumbra of about 50% magnitude covers the west part of CORS GNSS network, estimated from satellite PRN2. (**a**): time evolution of the TIDs wavelengths, (**b**,**c**): velocity vs. azimuth polar plots at intervals of half an hour, the continuity and amplitude of TIDs are coded by colors and the dot sizes respectively. (**d**–**h**): TIDs activity maps at 16:50 UT, 16:55 UT, 17:00 UT, 17:05 UT and 17:10 UT, the white arcs marked with percentages are the iso-penumbra lines on the IPPs at the altitude of 250 km. The diagonal white line is the trajectory of the umbra's center and the magenta line marks the local noon at the altitude of 250 km.

For instance in Figure 6, we show a measurement done with all the satellites and stations. From visual inspection, one can see that the wave forms follow the curvature of the umbra, and that the wavelengths are not uniform. In addition, in the east section of network (about 100°W to 80°W of longitude, and 28°N to 50°N of latitude) a set of ripple waves can be observed, that have a much lower wavelengths compared with the main ones that cover the whole continent. This idea of partitioning the network as a function of the scale of the disturbances allows for analyzing the ripples as medium scale TIDs, by dividing CORS into subnetworks with the geographic scale of 10° × 10° (latitude vs. longitude), see details in Section 4.5.

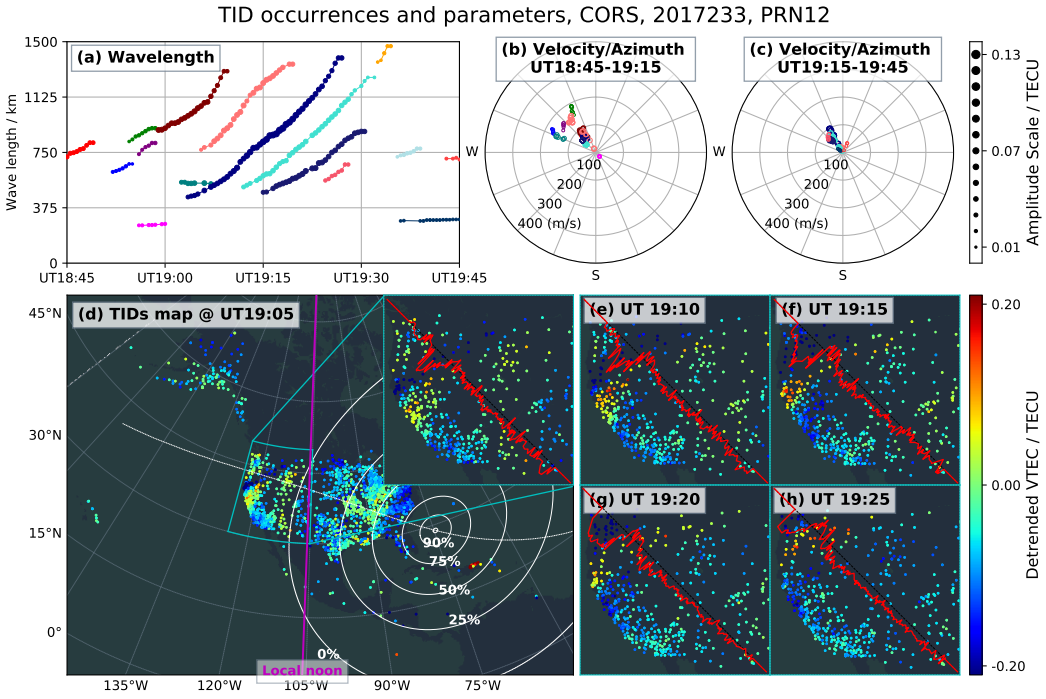

Figure 4. West coast sub network. (**a**–**c**): wavelength and velocity/azimuth plots. (**d**–**h**): lines of equal penumbra TID parameters plots when the penumbra of about 0% magnitude in the west part of CORS GNSS network, estimated from satellite PRN12 and TIDs activity maps at 19:05 UT, 19:10 UT, 19:15 UT, 19:20 UT and 19:25 UT. The plot is organized as in Figure 3.

4. Results and Discussion

In this section, we will analyze the diverse types of ionospheric disturbances generated during the eclipse transit at a height of 250 km. The analysis will be done both, by means of the ADDTID algorithm and by visual inspection of the maps. The TIDs that we detected (and visually verifed) show a wide range of features that depend on the elevation angle change, the footprint, size, azimuth and velocity of the umbra. We have structured the analysis of the generated TIDs, first following the temporal evolution of the eclipse and finally a global summary:

1. Time-varying TIDs analysis of the early and final moments of the eclipse observed from California in Section 4.1.
2. Simultaneous TIDs with multi-scale wavelengths presented during the middle stage of the eclipse observed from California in Section 4.2.
3. In Section 4.3, we summarize the detected multi-scale TIDs during the whole transit of the eclipse.
4. In Section 4.4, we show in detail the features of bow wave consisting of large scale TIDs, and in particular the estimated opening angles.
5. The medium scale TIDs in the penumbra are described in Section 4.5, such as partial circular waves, apparition of receding ripples among others.
6. In Section 4.6, a set of early MSTIDs at the east coast is detected before the arrival of penumbra.

4.1. Time Varying TIDs Wavelengths in the Early and Final Stages of Eclipse Transit

In this section, we will describe the temporal evolution of the TIDs in the early and final stages of the eclipse. The description will be carried out simultaneously, by means of the parameters detected with the ADDTID algorithm and by visual observation of the maps for verification purposes.

The disturbances that appear in the early and final stages of the eclipse, coincide with the distribution of the TIDs when the umbra either is about to enter the continent or to leave it. The eclipse-induced ionospheric perturbations would primarily be the consequences of the atmospheric cooling effect at all heights. However, the response of the ionosphere to the cooling due to the rapid variation of the penumbra is not well understood. As is shown in the model of Figure 2, where the lines of iso-penumbra and umbra (see computation details in Montenbruck and Pfleger [35]), are superimposed with the simulated global horizontal irradiance color map (see simulation details in Andrews et al. [36]). The consequence is that the movement of the shadow, generates fast space-varying and time-varying cooling effects at the atmosphere. This movement is in part, due to change in the grazing angle at the different stages of eclipse. The main feature is that for grazing angles of the umbra, the penumbra creates elliptic-like shadows of gradual obscuration. On the other hand, for vertical angles the shadows of the penumbra show less eccentricity. The geometry of the problem gives rise to a changing velocity of the penumbra shadows. That is, while the angle increases steadily, the velocity of change of the elliptical shadow of the penumbra will be high during the transition from grazing angles to medium angles.

As reported in Zhang et al. [14] and Sun et al. [16], the eclipse-induced ionospheric disturbances can be classified into two categories with distinct scales: (a) bow-shaped large scale TIDs and (b) medium scale TIDs of bow waves, originated respectively by in situ and not in situ gravity wave effects. In this subsection we will study both kinds of the disturbances in a separate subnetwork centered at California, (see in Figure 1). The California network is defined as a more restricted geographical area, which covers a smaller region, with a high density of stations allowing a more clear detection and modeling of the TIDs, because they can be locally approximated by a planar wave. Another reason we limit ourselves to this subnet is that for grazing angles, the distribution of TIDs will be very different across the continent, which could result in a mixture of different effects. The result of this change in angle, is the emergence of a set of TIDs, with a wavelength time evolution that follows a parabolic shape. This parabolic shape of the evolution in time of the wavelength is common to the entering and departing phases of the umbra and penumbra.

4.1.1. The Early Stages of Eclipse Transit

Figure 3 (GNSS observation of GPS satellite PRN2), shows the entry phase of the eclipse. Figure 3d–h show TEC maps of the west coast between 16:50 UT and 17:10 UT. Superimposed over these maps, we show the isopenumbra lines from 90% to 0% of obscuration, when the umbra is over the Pacific ocean. By means of the algorithm presented in Montenbruck and Pfleger [35], the lines of isopenumbra are depicted at an altitude of 250 km, and the measurements over the set of stations over the continent. The lower right part, shows a zoom of the TEC evolution at time intervals of 5 min. The upper part of the figure shows the time evolution of the TID wavelengths (Figure 3a) and the two polar plots of azimuth vs velocity (Figure 3b,c). Wavelengths, azimuth, velocity and amplitude are all estimated by the ADDTID algorithm. Please note that the azimuths and wavelengths given by the ADDTID coincide with the values that can be estimated at glance from Figure 3d–h. In addition we have overlaid on the maps, the projection of the detected points to a straight line with an inclination equal to the most common azimuth of the detected TIDs. Please note that the projection allows the visual inspection to determine the approximate wavelength of the disturbances and the propagation azimuth. As a supplement to Figure 3, we have posted on the Internet VTEC variation films during the eclipse in [37].

Next, we will describe the evolution of the TID estimated by means of the ADDTID algorithm and we will contrast it with the measured maps. Beginning at 15:55 UT, the penumbra contacts

the ionosphere over west US region, and from then on, increasingly covers this region. The time evolution of the TIDs in the early 30 min, show Medium Scale TIDs (MSTIDs) with a wavelength in the range of 250 to 300 km, a propagation following an azimuth towards the southeast. Please note that although the distribution of velocities is broad, most of the observations (75%) are concentrated in the range 150–300 m/s. The amplitudes during this time interval decreased from 0.08 to 0.02 TECU. The color-coding convention we have followed assigns a different color to each continuously detected TID sequence. The same colors have been assigned to the wavelength paths and points in the azimuth vs. velocity diagram. The MSTIDs detected during local morning hours show the typical daytime pattern in summer, mostly driven by solar terminator, see similar reports in Hernández-Pajares et al. [30]. At about 16:45 UT, the MSTIDs suddenly disappear, and a set of long wavelength TIDs emerge, that show a downward trend starting at a value of 1125 km. This change coincides with the arrival of the penumbra at a level of obscuration of 50–75%, as can be seen from the geographical distribution of the iso-penumbra lines at Figure 3d. The azimuth of the long wavelength TIDs moves 10 degrees to the east, and the velocity as seen in Figure 3c decreases to 150–50 m/s and the period decreases to a range of 3–0.75 h. This can be confirmed by visual inspection of Figure 3d–h. Meanwhile, the umbra above the Pacific ocean moves toward to east at speed of about 3000 m/s. Around 17:15 UT, 55 min after the onset of the penumbra reaches the network, the penumbra reaches a 50% obscuration, and the wavelength of the TIDs converges to a value of 400 km. As shown in Figure 5, this occurs a few minutes after the umbra contacts the California network.

The phenomena that we have described can be explained from the physical point of view in several ways (see discussion of the literature on this topic in the introduction). Zhang et al. [14] observed the penumbra-induced TIDs and recognized as the partial bow waves which should originate from the neutral atmosphere when the ground shadow is of about 50% magnitude. The time interval between the onset of TIDs and the time when the penumbra first arrives in California is compatible with the 0.5–1 h delay range of the onset of TIDs according to Liu et al. [12] and Nayak and Yiğit [15]. Another phenomena, that are observed in this paper are the bow waves and related disturbances, and the different delays in the apparition of the ionospheric disturbances. Shock waves are believed to originate from gravity waves in the middle atmosphere, due to the umbra moving at supersonic speeds. On the other hand, the penumbra that partially covers the solar radiation produces a cooling mechanism different from the umbra. This effect encompasses several frequency bands, Huba and Drob [17] indicate that the moon blocks the irradiance of ultraviolet light (uniform in the solar disk) in a similar way to light in the visual spectrum. In Kazadzis et al. [38], it is observed that a significant part of the ozone column decreases when the obscuration associated with darkness exceeds 70%. As the column variation in the ozone layer, absorbs most part of UV radiation, the cooling effects by the low obscuration penumbra were not enough to break the heat balance in the middle atmosphere. Therefore, these TIDs observed tens of minutes prior to the coverage by the 50% obscuration penumbra, might have a different origin. The global horizontal irradiance of the region covered by the umbra and penumbra is depicted in the diagram of Figure 2. The decreasing intensity of the irradiance from center outwards, generates different cooling effects, similar to a solar terminator, with a very fast diurnal variation. For instance, Huba and Drob [17] report the delayed variation of irradiance of X-ray and Extreme UV (EUV) because 10–20% contribution in these bands are generated at the solar corona, which is not covered by the moon. While the X-rays and EUV photons which are the primarily source of photoionization in the ionosphere, is occluded by the moon. On the other hand, Coster et al. [3] observed the TEC depletion follow with a short time delay the radiation distribution induced by the umbra and to the percentage of penumbra, and reported the penumbra-induced large scale TIDs activities could be originated in situ with the thermosphere. This explains the above mentioned set of long wavelength TIDs, that appeared suddenly when the coverage of the penumbra reached the 50% of obscuration, and the following convergence of the TIDs about a few minutes after the umbra reaches the network. Also is compatible with the ionospheric

disturbances reported by Le et al. [4], Müller-Wodarg et al. [39] and Sun et al. [16], which would be directly generated in thermosphere.

Figure 3 shows that the wavelength trajectory of long wavelength TIDs follows a descending parallel parabolic shape. This path is compatible with decreasing the distance between the isopenumbra lines. That is to say, the solar irradiance gradient increases as the angle of the shadow increases from 6 degrees to 40 degrees, with the consequent reduction in the rate of variation of the isopenumbra lines. At the same time, the direction of propagation (southeastbound) of TIDs is perpendicular to the isopenumbra lines over the California network. The cooling effect on the California area increases considerably as the angle and speed increases. This speed is supersonic at the heights where disturbances occur. In conclusion, this shows that the deceleration of the rate of change of the area of the penumbra and the decrease of the such area, is associated with a decrease of the wavelength of the TIDs. This happens in spite of the fact that the speed of the TIDs is slower than that of the umbra.

As for bow waves, the shape of the TIDs induced by the penumbra is consistent with bow waves of variable aperture in the south direction. One aspect to note is that the geomagnetic lines give rise to a slight deviation towards the equator due to the low geomagnetic activity, as mentioned in Section 2, see Coster et al. [3].

4.1.2. The Final Stages of Eclipse Transit

In Figure 4 we show, for the departing phase of the eclipse. For more details see the movie in [40]. The measurement has been made in the California subnet when the umbra is over the Atlantic Ocean, which results in a grazing angle of the penumbra. The parameters shown in the figure were estimated on the west part of CORS GNSS network, using the GPS satellite PRN12. The temporal evolution of the wavelength shows, for the departing phase, a complementary behaviour to that observed in the entering phase of the eclipse. The differences are due to the fact that the decrease rate of change of the elevation angle of the moon is not exactly the opposite of the entering phase of the eclipse (see Figure 2). On the other hand, the azimuth of the detected wavefronts is compatible with the direction of the isopenumbra lines over the network.

At about 19:35 UT the TIDs with increasing wavelength get weaker and finally disappear when the wavelength is over 1200 km. Subsequently, the activity of the disturbances decreases significantly, after which only very low intensity TIDs are detected. These disturbances have an azimuth opposite to that of the typical disturbances of this time of year.

The TIDs that have been detected show similarities with those of the initial stage, in the sense that the direction of propagation is perpendicular to the isopenumbra lines, the range of velocities is similar, and they are not significantly affected by the geomagnetic fields. A difference with respect to the TIDs of the initial stage of the eclipse is that the propagation is in the opposite direction to the movement of the shadow, which indicates that there may be no relation with the variation of the penumbra. In addition, these TIDs occur at the time when the shade is at its lowest, i.e., when the shadow leaves the California region, about 105 min after the umbra and about 85 min after the isopenumbra level of 50% leaves the subnetwork. This suggests that the fluctuations of the ionosphere are not due to the direct cooling effect in the thermosphere, but are upward gravity wave disturbances originating in the neutral atmosphere. Nevertheless the behavior of the TIDs differs from Coster et al. [3] and Zhang et al. [14], Chimonas and Hines [5] explains the above-mentioned behavior of disturbances by stating that long period atmospheric gravity waves cannot ascend from the point of generation at a sufficiently steep angle. From theoretical considerations, they conclude that the period of the disturbances is 3 to 4 h, which is in line with the results of the estimate we have made. The period of the TIDs detected in F region, increases gradually from 1 to 5 h. Similarly, in a study related to the 7 March 1970 eclipse, Davis and Da Rosa [9], in synchrony when the penumbra boundary (i.e., 0% area) left the network, observed westward TIDs in the form of decreasing amplitude shock waves with gradually increasing periods. However, the period of the TIDs estimated was of about 25 min, which was not consistent with the predicted long period in Chimonas and Hines [5].

4.2. General Description of the Multi-Scale TIDs (Medium and Large) in the Middle Stage of Eclipse Transit

In this subsection, we show the presence of the multi-scale TIDs, i.e., medium and large, measured from the California subnetwork.

Figure 5 shows the characteristics of ionospheric perturbations when the umbra crosses the California subnetwork. For more details see the movie in [37]. The umbra contacts the atmosphere above this region at a height of 250 km at about 17:11 UT and leaves the subnetwork at about 17:42 UT. As mentioned in Section 4.1 during the early stage, the set of parallel wavelength-varying TIDs from 17:00 UT follow a downwards trajectory, converging towards a medium scale wavelength TID of about 400 km, 4 min after the arrival of the umbra. Almost simultaneously, with a slight delay due to the response of the ionosphere (see Figure 5a), a disturbance suddenly appears with a wavelength of 1125 km at about 45 degrees of azimuth, nearly 90 degree to the north of the medium scale TID azimuth. This perturbation corresponds to the three segments of the trajectory observed at Figure 5a. Please note that the trajectories of large-scale disturbances are reflected on the projection (in red) in Figure 5e–h, as almost two cycles of a sine wave with a wavelength compatible with 1200 km.

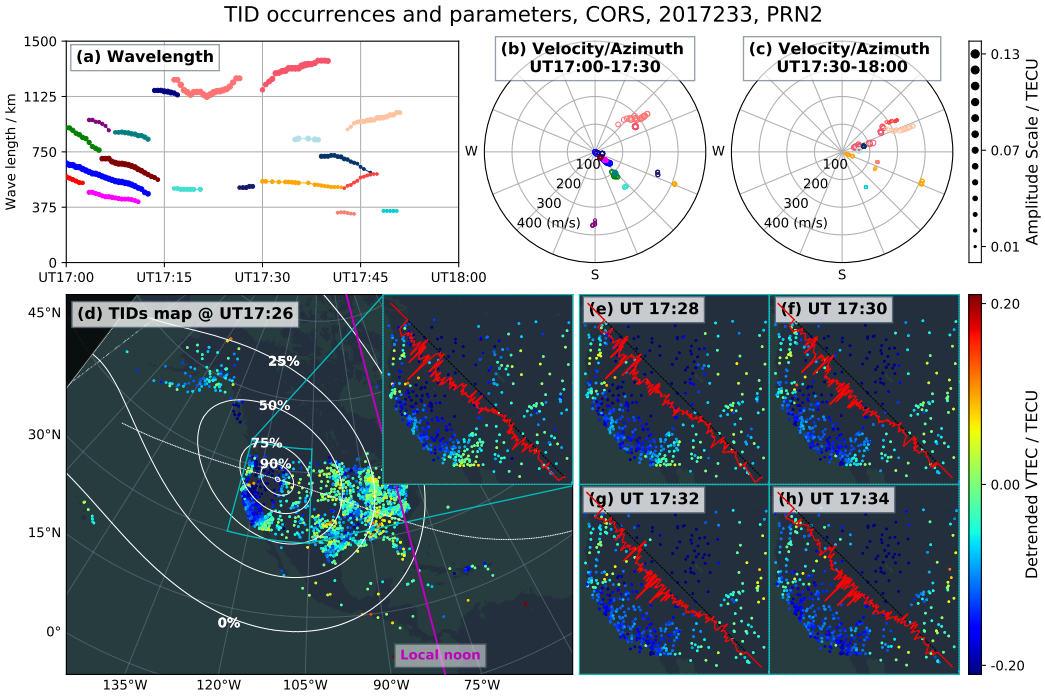

Figure 5. Time-variation plots of the TIDs parameters, when the umbra covers the west part of CORS GNSS network, estimated from satellite PRN2, organized as Figure 3. TIDs activity maps shown at 17:26 UT, 17:28 UT, 17:30 UT, 17:32 UT and 17:34 UT.

Both disturbances persist between 17:15 UT and 17:45 UT, the long scale disturbance with an amplitude of about 0.11 TECU and the medium scale of about 0.05 TECU for other. The spread in terms of azimuth of both perturbations shifts several degrees towards the east, which is compatible with the lines of equal penumbra and perturbations shown in Figure 3. The disturbance of longer wavelength can be found by visual inspection in Figure 5.

Although the observed velocities of both sets of TIDs are lower than the typical velocities for large and medium scale TIDs, there is a consistency, in the sense that the large scale TIDs propagate at a double speed compared to the medium scale waves.

Note also, that of the size and distribution of the stations is lower than the area covered by the bow wave, therefore only one of the branches of the bow wave is detected in the figure. Another effect that can be observed at the maps and the wavelength vs. time figure (Figure 5), is that the amplitude

of the large scale TIDs is greater than in the case of the medium scale TIDs (note that the amplitude is coded by the size of the dots). An additional observation from this Figure, is that the azimuth of the TIDs does not coincide with the trajectory of the eclipse on the maps. This might be related to the movement of the bow wave fronts both in large and medium scales. In the figure there are also disturbances that appear in advance of the umbra.

These medium scale TIDs are a response of the ionosphere to the transition from the penumbra to the umbra, which generates the ionospheric wave in situ. Whereas long scale TIDs are also due to the effect of the umbra on the ionosphere, with delay appearing after the umbra has already moved away [16]. These TIDs originate in part due to the cooling effect of the umbra's shadow, creating gravity waves in the thermosphere.

4.3. Description of Ionospheric Disturbances during the Eclipse

In this section will characterize and describe the ionospheric disturbances related to the bow waves during the transit of the eclipse.

By visual inspection, in the maps plotted at Figure 6a, one can see a bow wave that varies gradually at the different stages of the eclipse (see more details in [41]). In the three maps, in addition to the bow wave, it is also possible to observe disturbances in advance of the umbra, and in the wake of the umbra (see similar observations in Zhang et al. [14]). The shape of the waveforms of the disturbances are akin to the lines of iso-penumbra in Figure 2. That is, the disturbances in advance of the umbra follow the shape of the lines of iso-penumbra. The disturbances in the wake of the umbra show an elliptical curvature following the shape of the lines of iso-penumbra, and also ripples (Figure 6a at 18:45 UT) of lower wavelength with a complementary curvature.

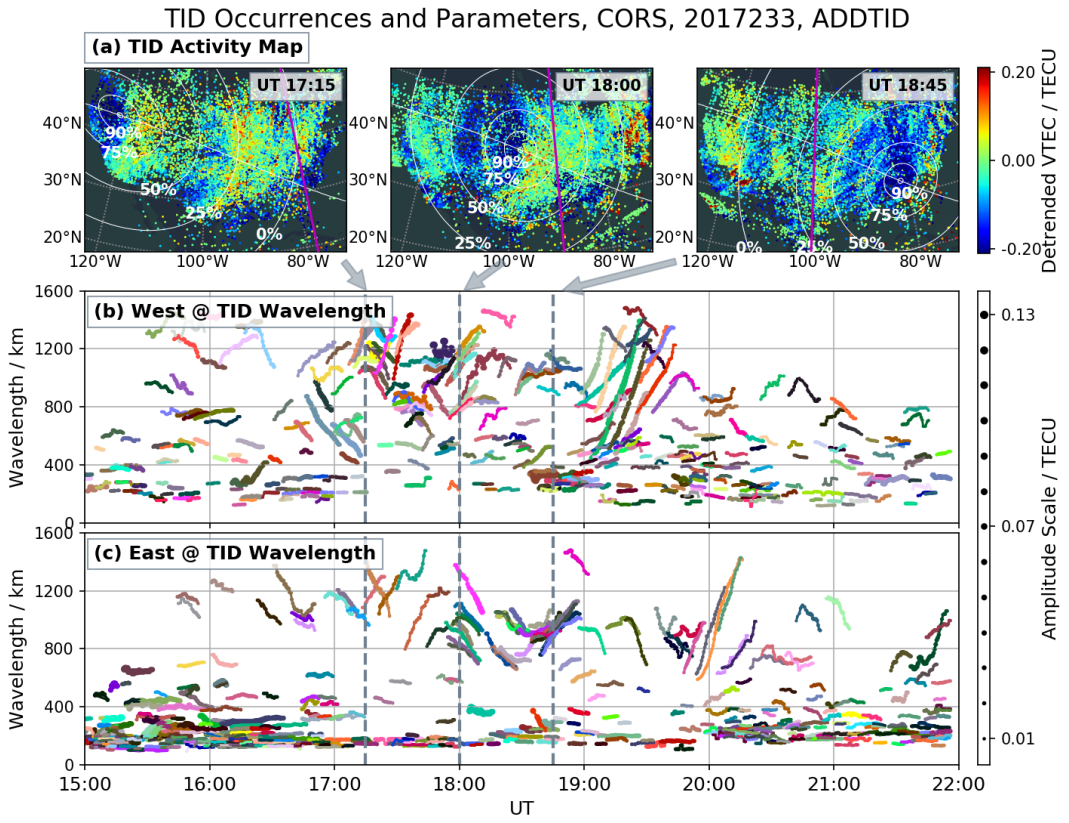

Figure 6. (**a**): TIDs activity maps at 17:15 UT, 18:00 UT and 18:45 UT, similar display scheme with the TIDs map in Figure 3. (**b**,**c**): Wavelength time evolution for the west subnetwork (**b**) and east subnetwork (**c**), point color and size code organized as Figure 3. The grey arrows pointing to dashed vertical grey lines indicate observation time.

In Sections 4.1 and 4.2, we show on the west coast, the occurrence of disturbances at medium and large scales, ranging from a few hundred to more than a thousand kilometers. This phenomenon can be seen on the maps in Figure 6a. In Figure 6c, we also show that the measurements done on the east coast, follow with a delay, the shape of the wavelength evolution on the west coast.

These ionospheric disturbances during the eclipse appear as patches of 2D non-concentric near circular wave patterns, moving horizontally. Since the curvature of the TIDs over the region of each network is small enough, the ADDTID algorithm will be able to correctly detect the disturbances and estimate their characteristics. To better understand the spatial-temporal characteristics of large-scale ionospheric disturbances and their relationship to the eclipse, the estimation has been made with the entire CORS network. That is, the GNSS data used in the ADDTID algorithm correspond to the two subnetworks into which we have divided the CORS network (see Section 2). Please note that each subnet is at least twice the maximum wavelength. Figure 6b,c, show the time evolutions of the TID wavelengths respectively detected from west and east subnetworks of the CORS network.

The disturbance in advance of the umbra that can be understood as an early bow wave. The origin is due to the changes in temperature generated by the increasing penumbra, giving rise to disturbances of lower intensity in comparison with the one that was generated by the umbra [4,39]. As the penumbra moves at a higher speed for grazing angles, the perturbation due to the eclipse appears some time before the umbra reaches the region covered by the stations. Also, follow a distribution similar to concentric ellipses, which is due the change on the angle of the umbra over a sphere (see for instance the diagram in Figure 2 and the previous discussion in Section 4.1). These disturbances in advance to the bow wave can be observed clearly in Figure 6a at 17:15 UT.

The measures done at the stations over the west subnetwork show that the typical pattern of MSTID at this time of the year, disappear completely, while on the east subnetwork, which is at the other side of the continent, they are reduced in number. In both cases the behaviour of the large scale TID (LSTID) change, in case of the west subnetwork there is a noticeably decrease in the wavelengths of these disturbances. With a delay of about half an hour, the same phenomenon appears on the east subnetwork. A remarkable aspect is the continuity between the MSTIDs and the LSTIDs, which can be seen in Figure 6a or zoomed at Figure 3. Also it can be seen in Figure 7c,d from the azimuth vs. velocity plot that the direction of the large scale disturbances in consistent with the direction of propagation of the umbra. This continuity of the transition between MSTIDs and the LSTIDs and vice versa can be observed at both networks. As for the LSTIDs propagation (Figure 6a at 17:15 UT), the disturbances follow the lines of iso-penumbra and propagate in the direction of the movement of the eclipse, except at the east edge of the continent, where the angle varies slightly, perhaps due to propagation delay. Around 18:00 LSTIDs with similar behavior appear, with a greater opening angle, and a direction that follows the movement of the umbra, see the more details in Section 4.4.

The complementary behaviour is shown in Figure 6a at 18:45 UT, where we observe the disturbances that appear when the umbra is over the west coast. In this case we observe LSTIDs to the west of the umbra that follow the shape of the lines of iso-penumbra, with wavelengths that increase slowly from 700 km to 1300 km. In addition, at the same time, MSTIDs of lesser wavelengths, with a front waves with a curvature of opposite sign. These MSTIDs have a wavelength of about 200 km, and on the map appear as ripples that can be observed at the west of the umbra. This transition can be seen more clearly in the zoom at Figure 4a, and the azimuth vs. velocity plot of Figure 4b,c, shows that the perturbations propagate in opposite direction to the propagation of the umbra. In Section 4.5 the MSTIDs which correspond to the ripples are explained in detail.

4.4. Description of the Large Scale Ionospheric Perturbations Related to Variable Angle Bow Waves

In this section we extend the characterization done in Section 4.3 of the behaviour of the large scale ionospheric disturbances (i.e., LSTIDs) during the eclipse transit. The behaviour of the LSTIDs during the eclipse is summarized in Figure 7, in which we show time-aligned: (a) wavelength path

(Figure 7a,b) and (b) velocity vs. azimuth polar plots (Figure 7c,d). This diagram will allow us to understand the relationships between these characteristics throughout the eclipse transit.

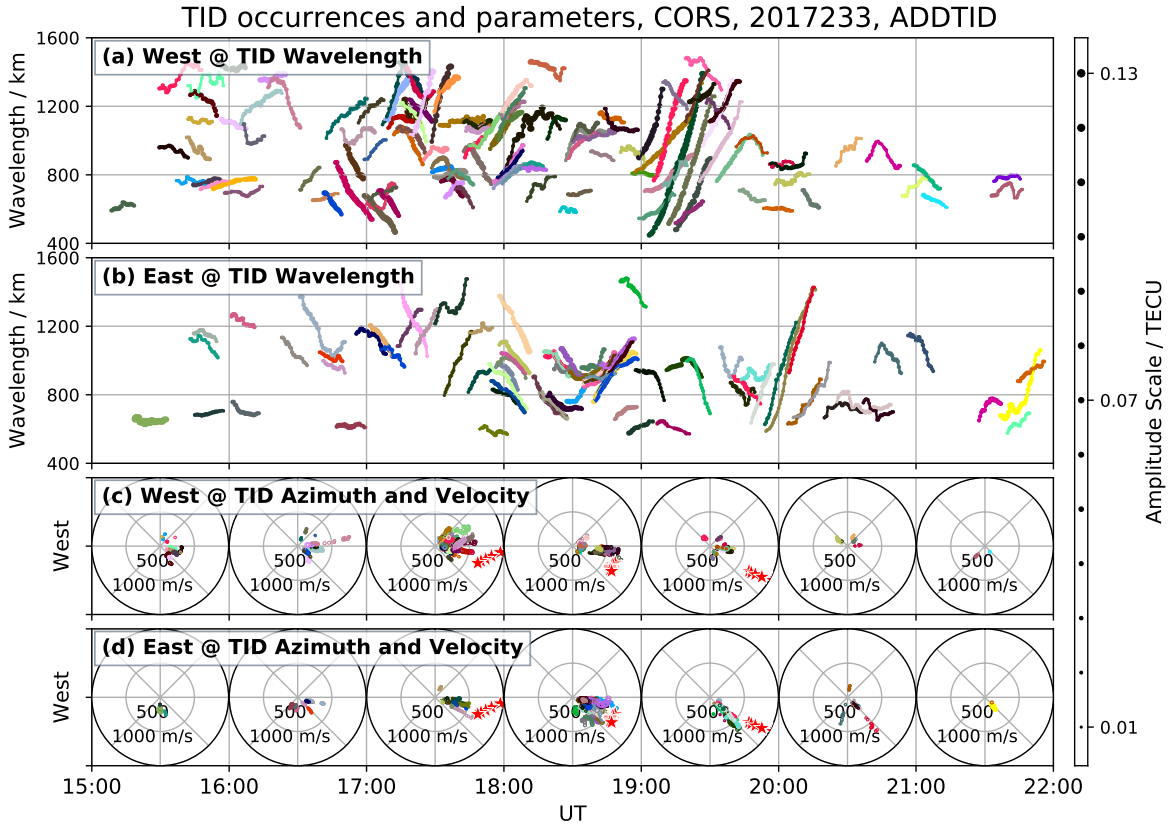

Figure 7. Behavior of the LSTIDs during the transit of the eclipse (Time aligned). (**a**,**b**): time evolution of the wavelength of the LSTIDs, (**c**,**d**): Azimuth vs. velocity polar plots at intervals of one hour, red stars for the azimuth vs. velocity of umbra. The dot color and size (right bar) coding follows the convention in Figure 3.

The LSTIDs shown at Figure 7a,b have similar wavelengths and velocities as the typical large scale TIDs [42], nevertheless the directions as shown at Figure 7c,d are different, following the azimuth of the umbra center, which is denoted in the polar plots with the red stars.

Before the arrival of the eclipse to the continent, the LSTIDs exhibited a quiet behaviour, characterized by low amplitude and propagation mainly in the equator-east direction. The duration of the disturbances was less than 15 min, the speed was low of about 100–200 m/s and with long periods in the order of 1.5–2 h. At about 15:56 UT, the penumbra arrives first at the ionosphere 250 km above the west coast of US, from then on, the penumbra increasingly covers this region. At the same time the number of LSTIDs increases. During the time interval 16:10–17:15 UT, when the 10% iso-penumbra line reaches the western US, the properties of the TIDs change. The LSTIDs now head eastwards, with a marked increase in the speed (over 500 m/s). The wavelengths of the LSTIDs, decrease from about 1500 km to 800 km, and then increase above 1200 km. Please note that the delay between the west and east US, in terms of the evolution of LSTIDs, is approximately half an hour, which is consistent with the delay due to shadow propagation. This delay was computed from the shape of the wavelength trajectory observed in the figure, in particular from the position of the minimum of the parabola that is repeated at each coast.

At about 17:15 UT, a large number of LSTIDs suddenly appear, a couple of minutes after the umbra arrives the west US. At the west network between 17:15 UT and 18:05 UT (about 18:05 UT, the umbra leaves to the west part of US), the wavelength path of the LSTIDs shows a parabolic shape, the edges of this trajectory are determined by the entering and leaving phase of the penumbra (see comments

in Section 4.1). The disturbances show an eastward propagation, with an azimuth scattering of 60 degrees and a speed range between 300 and 700 m/s.

In the velocity-azimuth diagram, the points associated with the bow wave are distributed in a fan shape, which corresponds to an opening angle of the bow of 120 degrees, and a propagation with an azimuth of 10 degrees. This fan also indicates the speed of each of the branches of the bow. The bow wave follows the path of the umbra, which at this moment has an azimuth of roughly 10 degrees south east and a velocity in the range of 1500–670 m/s in Figure 7c.

After leaving the western network, the activity of the LSTIDs gradually weakens until they disappear. A similar behaviour with a time delay, is visible in the eastern network. However, there are differences in the distribution and properties of LSTIDs on the east coast compared to those on the west coast. When the umbra covers part of the eastern subnetwork between the 18:05–18:50 UT, the angle of opening of the bow wave increases to about 135 degrees, while the umbra speed decreases to 650 m/s. At this time, the bow wave in the eastern subnetwork shows a global deviation of 30 degrees south, which is compatible with the azimuth changes of the umbra movement. Please note that the direction of propagation of the bow wave, along with the two branches of the bow, follows the movement of the umbra, with an deviation in azimuth. This deviation is about 10 degrees north east at 17:00–18:00 UT, and about 5 degrees south east at 19:00–20:00 UT. The low activity of the geomagnetic field has little influence on the movement of the ions, so the deviation may be due to the variation in the eccentricity of the ellipses resulting from the penumbra, and to the rotation of the ellipse axes. The deviation and lines of equal obscuration can also be seen on the TID activity maps.

In Figure 8, we show the relationship between the opening angle of bow wave with the velocity of the umbra. The figure shows in green the measurement made by visual inspection on the maps and in grey the estimation using the ADDTID algorithm, and also in blue a nonlinear fit of the ADDTID opening angle to smooth the estimation errors. The manual measurement on the maps was performed prior to the measurement obtained from the ADDTID algorithm. This confirms that the ADDTID algorithm can detect wavefronts and matches the approximate measurements manually estimated. The order of the measurements is methodologically correct, as it avoids biases due to having observed first the measurement from the algorithm. This order is justified, was because once the manual measurement was performed, a posteriori check by means of the ADDTID was made to confirm whether the manual measurement was correct. The velocity of the umbra is computed by the algorithm Montenbruck and Pfleger [35], and the time evolution follows a concave up parabolic shape. During the transit over the CORS network, the part corresponding to the highest acceleration of the umbra was located outside the network. Please note that, as the velocity slows, the degree of opening of the bow wave increases for both two measurements. The moment when the umbra velocity reaches a minimum is about 18:29 UT (see the mark in Figure 8), which coincides with the moment when the iso-penumbra line of 0% is completely within the territory of the United States. The decrease in the opening angle of the bow wave observed with about 3–5 min delay, is due to the increase in the speed of the umbra. The estimated opening angle shows a higher noise from 19:00 UT on, when the umbra has already left the continent and is now on the Atlantic Ocean, and thus the two arms of bow waves of LSTIDs are not completely observed by CORS network any more, as shown in Figure 4. Therefore the measurement by means of visual inspection is reliable only until 18:30 UT. The LSTIDs corresponding to the measurements in Figure 8 show the small delay with respect to the umbra, and propagate at a speed greater than the speed of sound in the middle atmosphere. Both these two characteristics are consistent with the findings in Coster et al. [3] and Zhang et al. [14]. This behaviour does not correspond to the gravity waves induced by the eclipse in the middle atmosphere [5], but to the shock waves generated in the thermosphere, with a speed compatible with the acoustic velocity [16].

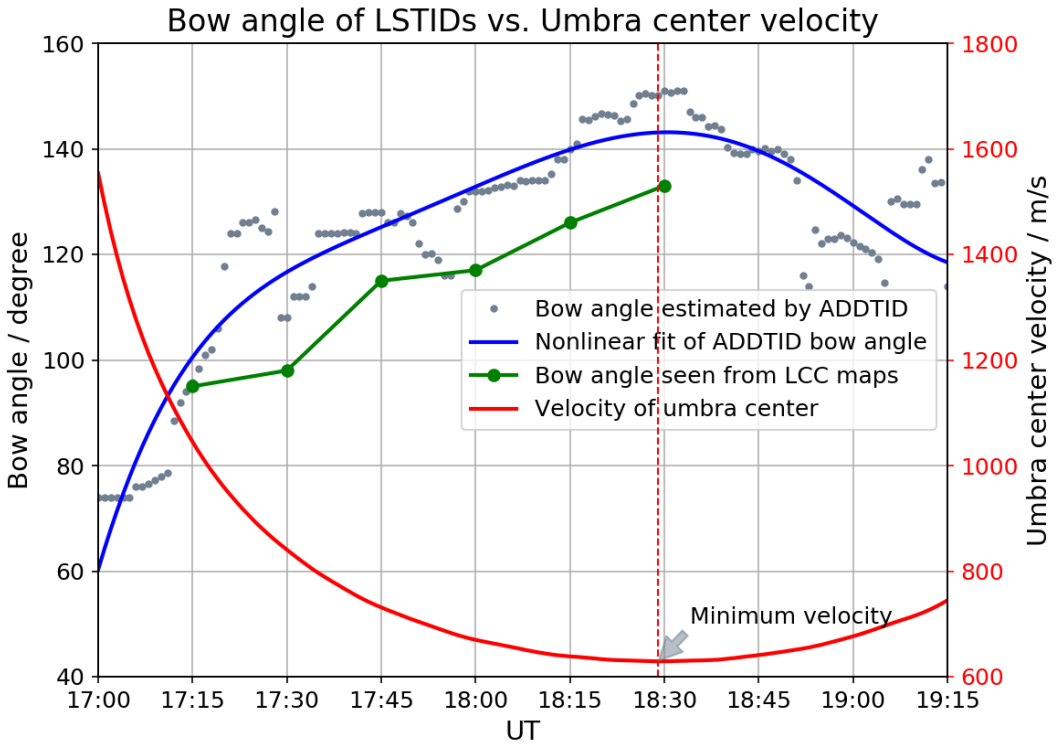

Figure 8. Time evolution of bow opening angle vs. the velocity of the umbra. Grey dots represent the estimated opening angle by ADDTID. The blue line is the nonlinear fit of the estimated opening angle. The green line for visual estimation of the opening angle from the Lambert Conformal Conic projection (LCC) maps, and red line for the velocity of umbra. Red dashed line pointing the time when the umbra velocity reaches minimum.

4.5. Variable Angle Bow Wave Consisting of MSTIDs Induced by Eclipse

As mentioned in the previously, at around 17:15 UT, several large-scale disturbances cover the entire continent, and the large-scale disturbances are present during the whole transit, including an overlap with different local MSTIDs. This can be seen in Figure 6a maps, which show the fluctuation of the detrended VTEC. As can be seen in Figure 6b,c, TID wavelengths range from hundreds to thousands of kilometers. From the maps measured between 17:15 UT and 18:00 UT, the wavefront near the umbra displays a V-shaped wedge shape, with an opening angle that increases with time. Also large-scale disturbances can be seen in advance of the umbra. The distribution over time of the disturbances on the continent can be regarded as the superposition of non-concentric circular waves of different radii. In addition, the ripples are observed to the left of the umbra on the 18:45 UT map (see Figure 6a). These ripples were detected automatically by the ADDTID algorithm and the wavelength (see Figure 6b,c) and azimuth estimation coincide with the measurements made over the map.

To give a more complete description of the bow wave and the ripples at the west of the bow, we will introduce geodetic information, by overlaying on top of the map, local azimuth vs velocity plots computed at $10^\circ \times 10^\circ$ grids of latitude-longitude. The size of the grids is more than two times of the typical wavelengths of MSTIDs. The size of this grid of plots assures that the plane wave approximation done in the ADDTID will be valid (see for instance the detection of circular wave by an approximation by means of a planar wave model in Yang et al. [22]).

Since the MSTID characteristics vary in time and space (see detection in Section 4.3), an analysis was performed in a grid, as shown in Figures 9 and 10. These grids, show the local direction of the MSTIDs that appear as waves in the penumbra area behind the umbra, which as discussed in the previous section, could be originated by the acoustic gravity waves in the middle atmosphere.

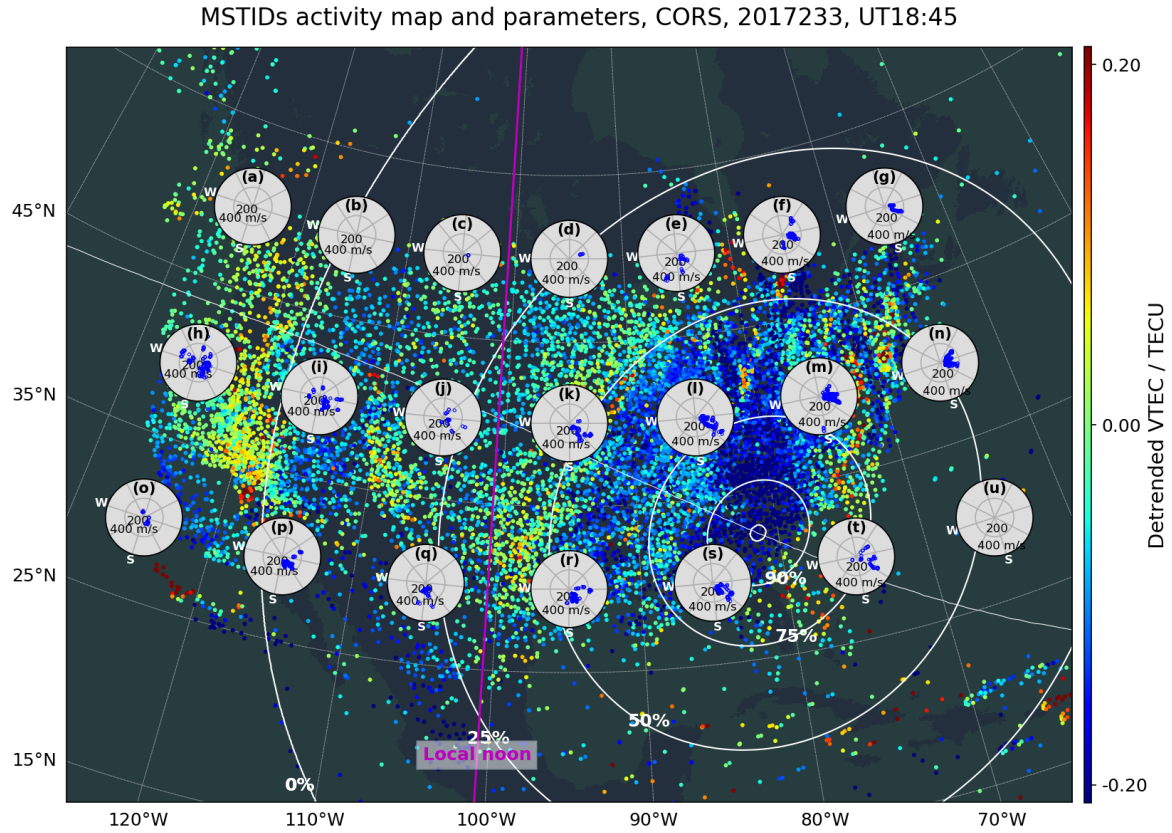

Figure 9. TID activity at 18:45 UT. Grid of the azimuths (in degree) vs velocities (in m/s) of TID estimated inside subnetworks of $10^\circ \times 10^\circ$ longitude - latitude. The each subplot is labeled with a letter at the top. In white, iso-penumbra lines at percentages that range from 0% to 100%. The magenta line shows the local noon meridian at height of 250 km.

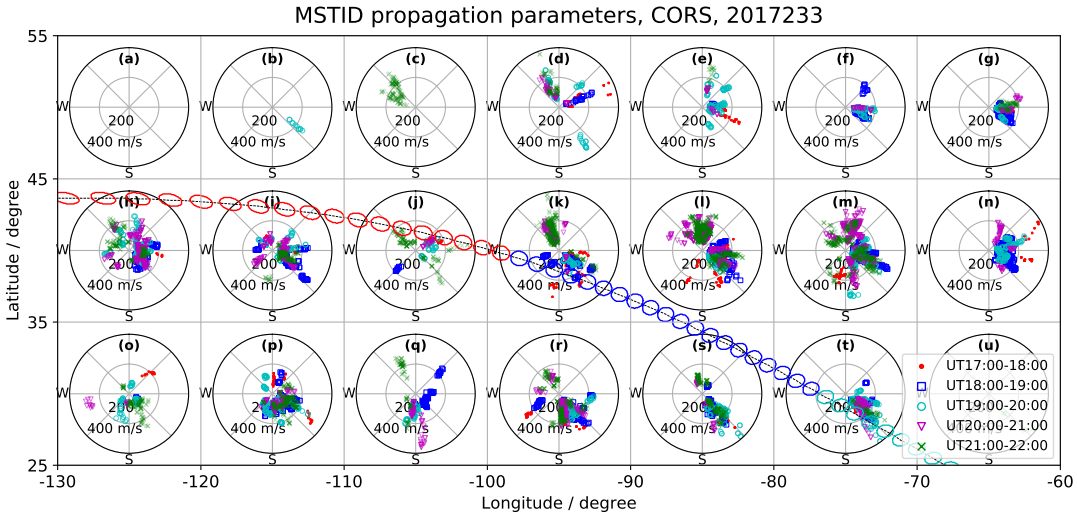

Figure 10. Grid of polar plots of MSTIDs in the 5 h interval, 17:00–22:00 UT superimposed over the US CORS network. The network is divided into $10^\circ \times 10^\circ$ longitude-latitude cells. The trajectory of the umbra, is marked by a series of ellipses, one every three minutes, and is divided into intervals coded by color. The color code is: red for 17:00–18:00 UT, blue for 18:00–19:00 UT, cyan for 19:00–20:00 UT, magenta for 20:00–21:00 UT, green for 21:00–22:00 UT.

Figure 9 shows at 18:45 UT the overlap of the detrended VTEC map, with the azimuth versus velocity diagrams of the locally detected MSTIDs. In the lower right of the map, is clearly visible

the shape of the bow wave from the thermosphere. On the other hand, the ripples appearing in the regions covered by penumbra greater than 50% and with a delay of tens of minutes behind the umbra are compatible with the description given at Chimonas and Hines [5]. The azimuth vs velocity plots adjacent to the ripples labeled (upper part) with the letters (e), (k), (l), (r) and (s) show clearly the propagation azimuths of the ripples which could be the short period components of the bow wave originated from middle atmosphere, see the similar reports for the long period components at the final eclipse stage in Section 4.1. The dominant velocity is in the range between the 200 m/s and 350 m/s. Furthermore, the azimuth vs. velocity polar plots on the east side of the umbra, such as (f), (g), (m) and (n), show medium scale disturbances in advance of the umbra, with azimuths compatible with the lines of iso-penumbra, which could be the time-varying ionospheric waves generated in the ionosphere, see the previous description of the early eclipse stage in Section 4.1.

Another way to analyze the middle scale ionospheric disturbances due to eclipse transit is by means of the diagram shown in Figure 10, where we show a grid of azimuth vs. velocity diagrams, ordered geographically, in which disturbance detection is done locally inside each $10^\circ \times 10^\circ$ section. In contrast with Figure 9, where we show a snapshot at 18:45 UT, in Figure 10, we show all the detected MSTIDs in the interval 17:00–22:00 UT, which includes the whole transit above US and in two hours after the transit. In the figure we also show the eclipse path superimposed over the azimuth vs. velocity diagrams. The path is marked by means of elliptical to circular shapes spaced temporally at the 3 min intervals. Please note that in each interval of one hour, the color is the same, but the shape has been designed so that it follows the area of the umbra. Therefore, the shape changes from highly elliptical at the upper left of the plot to almost circular at the bottom right, reflecting the inclination of the shadow of the moon with respect to the earth, simultaneously with the position over the continent. The color code that has been used in the azimuth vs. speed graphs follows the code represented in the path, so it can be seen how the umbra at any given time affects the entire US region. Please note that each azimuth vs. velocity diagram is labeled by a letter at the top. The figure shows the MSTID activities in each subdivision of the US CORS network when the umbra passes over the ionosphere at an altitude of 250 km.

Next, we will analyze by means of this figure, the distribution of the MSTIDs for each interval in which the path has been divided.

In the early interval (17:00–18:00 UT), the detected MSTIDs (coded in red), show patterns that differs across the entire network. During this interval, in Figure 7, one can observe a bow wave consisting of LSTIDs along the supersonic umbra. However, as for MSTIDs in Figure 10, no bow wave is detected along the umbra trajectory, just an irregular activity in the lower part of the trajectory and no detectable activity in the upper part. Meanwhile, in advance to the umbra and geographically more to the east (see subfigures (d) and (k) corresponding to the east part), we detected MSTIDs that show two partial branches of a bow-shaped disturbance, with azimuth angles of 50–70 degrees on the north side and 100–160 degrees on the south side, giving an angle of about 90–100 degrees, which compatible with an advance response to the southeastward umbra. Also have speeds in the range 150–250 m/s, wavelengths of about 180–250 km, and periods of about 20–50 min. This bow wave in advance of umbra, appears with transient delay of the penumbra, could originate from the thermosphere, as explained in Section 4.1.

During the middle stage when the umbra passes across US (18:00–19:00 UT), the MSTIDs (coded by blue triangles) appear in most of grid subplots. The MSTIDs in eastern subplots show a behavior consistent with the bow wave at the early stage. However, the western part and the part around the transit with southeastward direction (azimuth angles of 45–225 degrees), there are the partial wavefronts of the circular waves as ripples in the penumbra area, see Figure 9. These southeastward MSTIDs approximately pointing at the transit of umbra, have the following features: 100–300 m/s velocity, 200–400 km of wavelengths, and 30–70 min of periods, with a delay of more than tens of minutes with regard to the umbra. These MSTIDs show compatible propagation parameters with

Nayak and Yiğit [15]. The origin of these MSTIDs [5] could be the middle atmosphere by way of short period components of bow wave.

At the final stage of the eclipse above US (19:00–20:00 UT), the umbra is leaving from the continent, the delayed MSTIDs show an irregular distribution of the estimated parameters even in a same grid region. Besides most MSTIDs with southeastward directions, the other parts with similar velocity distribution but propagate to the northwest. Please note that the northwest MSTIDs show wavelengths greater than 350–550 km and periods longer than 60–100 min. These northwest MSTIDs have larger scales than the southeast waves. These patterns continue in the two hours after the ionosphere above US the umbra has leaved the continent (20:00–22:00 UT, i.e., 14:00–16:00 LT), when the MSTIDs particularly in the central subnets of US show omnidirectional azimuths as potential clues of circular waves. MSTIDs in the north subfigures show the northward propagation. The distribution of wavelengths and periods of these MSTIDs show consistent characteristics within the interval of 19:00–20:00 UT, i.e., the full northwestward (westward/northwestward/northward) MSTIDs have larger wavelengths and longer periods than the full southeastward (southward/southeastward/eastward) MSTIDs. The full northwestward MSTIDs would be the long period component of the bow wave, and the full southeastward MSTIDs might be the short period component of the bow wave, which originates from the middle atmosphere [43]. Furthermore, as for the long period components of bow waves, the northwestward MSTIDs appear approximately 1.5–3 h after the umbra departure, compared with about 30–60 min delay of the short ones.

4.6. Early MSTIDs at the East Coast, before the Penumbra Reaches the West Coast

In Figure 11 we show the presence of MSTIDs which show a behaviour that differs from that of the typical summer season. The propagation of normal MSTIDs of this season occurs in this season of the year during the night, following a west/polar-west/equator-west direction, while the presence of MSTIDs during the day is almost non-existent, see Hernández-Pajares et al. [30]. As shown in the polar diagrams, there are two groups of MSTIDs propagating in an eastward direction, with a low intensity between 0.04–0.06 TECU. The map at the top right shows the local noon by means of a magenta line. Note both of the MSTIDs exhibit steady behavior with regard to wavelength and azimuths between 15:40 UT (∼10:10 LT) and 17:30 UT (∼12:00 LT). The effect of the solar terminator is very weak at this moment. These MSTIDs indicate two clear directions of propagation one towards the equator-east, and the other in a polar-easterly direction. It is interesting to note that the polar-east direction is present during the whole interval. Please note that the effect of the magnetic field in the horizontal direction is small, because the azimuths are almost perpendicular to the geomagnetic lines. An explanation of why the MSTIDs are so seldom, and difficult to detect during daytime at summer, is given by Kotake et al. [44], that point out the upward acoustic gravity waves as the potential origin of the daytime MSTIDs. This is because the disturbances cannot propagate through the region of the steep temperature gradient near the mesopause in summer, thus the possibility of gravity waves causing MSTIDs would be further decreased at local noon.

One possible interpretation of the polar diagram (Figure 11c) would be that each of the propagation directions actually corresponds to the plane wave approximation of each of the arms of a soliton wave that advances ahead of the shock wave which originate from the thermosphere.

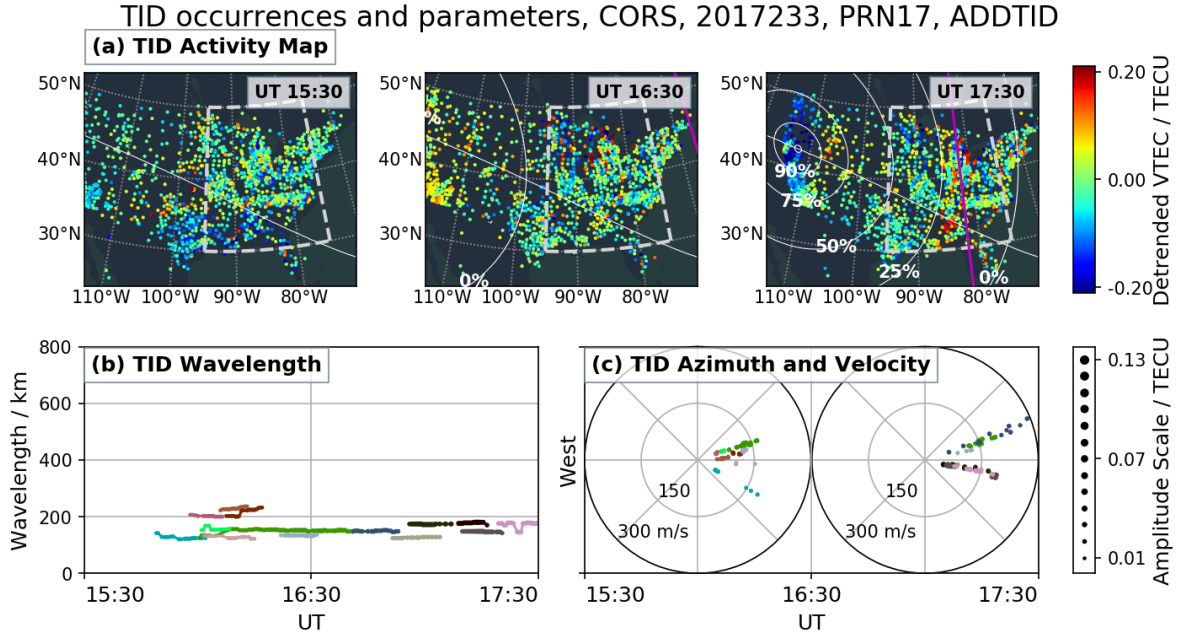

Figure 11. MSTIDs, over the eastern US, with propagation in the east direction. (**a**) Detrended VTEC maps (in TECUs), where the MSTIDs are visible for three snapshots at 15:30 UT, 16:30 UT and 17:30 UT, (**b**) Time evolution of the MSTID wavelengths of the subnetwork in white dashed rectangular, (**c**) Polar plots at intervals of one hour for MSTID azimuths vs. velocities, organized as Figure 3.

5. Conclusions

In this work we have described the diverse types of ionospheric disturbances that were generated during the US solar eclipse of 21 August 2017. The multi-TIDs detection technique, Atomic Decomposition Detector of Traveling Ionospheric Disturbances (ADDTID), has been used to automatically characterize the disturbances, see Yang et al. [22]. These disturbances show a rich set of different features related with the changing angle of the umbra with respect to the surface of the earth, such as the footprint, size, azimuths and velocity of umbra. Due to different patterns of behavior, the TIDs in this work have been categorized into the following phases: (a) The time-varying TIDs observed in the early stage, beginning with the arrival of penumbra with 50–75% obscuration. These TID wavelengths show a global downward trend from 1125 km, and finally converge at 400 km about 4 min after the umbra arrival, when a new set of large scale TIDs appear suddenly. The time-varying and large scale TIDs show respectively propagation in the southeastward and northeastward directions and are consistent with the umbra movement. These TIDs might originate from the thermosphere. (b) Another set of time-varying TIDs was detected at the final stage when the penumbra was leaving the West coast. With increased wavelengths, these TIDs show the periods from 1 up to 5 h, and appear with a delay of about 1.5 h after the departure of the umbra. The TIDs could be the long period component of the bow waves originating at middle atmosphere. (c) The global LSTIDs illustrate the consistent bow wave behavior with a variable opening angle. The location and appearance of the in situ bow waves respectively follow the umbra and penumbra movement with transient delays. In particular, the opening angle of the bow related to the umbra reaches a maximum at about 3–5 min after the minimum of the velocity of umbra center at height of 250 km. (d) Despite having similar wave parameters, the two MSTIDs depict two kinds of bow wave characteristics at different locations and times. For instance, the in situ MSTIDs occurs in advance to the umbra, whereas the others from middle atmosphere present in the penumbra after the umbra departure. (e) As a possible effects to ionosphere, the MSTIDs at the east US might be the soliton wave of the bow waves.

In the future, we plan to further improve the wave detection model in order to better characterize the various wave fronts of bow waves in the ionosphere, also developing a robust discrimination tool

to recognize disturbances related to different bow waves, and explore the determining technique of the bow wave parameters by means of the detected ionospheric disturbances.

Author Contributions: Conceptualization, H.Y., E.M.M. and M.H.-P.; Methodology, H.Y., E.M.M. and M.H.-P.; Software, H.Y., E.M.M. and M.H.-P.; Validation, H.Y., E.M.M. and M.H.-P.; Formal Analysis, H.Y., E.M.M. and M.H.-P.; Resources, H.Y.; Data Curation, H.Y.; Writing—Original Draft Preparation, H.Y. and E.M.M.; Writing—Review and Editing, H.Y., E.M.M. and M.H.-P.; Supervision, E.M.M. and M.H.-P.

Funding: This work has been supported by the 2017 SGR-0851 grant of the Generalitat de Catalunya. Also was partially supported by the project TEC2015-69266-P (MINECO/FEDER, UE). This work has been supported by the scholarship from China Scholarship Council (CSC) under the grant CSC No. 201508390017.

Acknowledgments: We acknowledge the GPS data of CORS are provided by the National Geodetic Survey (NGS), NOAA, US. All the code of this project was done in Python using the machine learning library scikit-learn. The data for this paper are available and they can be requested from any of the authors in particular from Heng Yang and Enrique Monte-Moreno.

Conflicts of Interest: The authors declare no conflict of interest.

References

1. Salah, J.; Oliver, W.; Foster, J.; Holt, J.; Emery, B.; Roble, R. Observations of the 30 May 1984, annular solar eclipse at Millstone Hill. *J. Geophys. Res. Space Phys.* **1986**, *91*, 1651–1660. [CrossRef]
2. Stankov, S.M.; Bergeot, N.; Berghmans, D.; Bolsée, D.; Bruyninx, C.; Chevalier, J.M.; Clette, F.; De Backer, H.; De Keyser, J.; D'Huys, E.; et al. Multi-instrument observations of the solar eclipse on 20 March 2015 and its effects on the ionosphere over Belgium and Europe. *J. Space Weather Space Clim.* **2017**, *7*, A19. [CrossRef]
3. Coster, A.J.; Goncharenko, L.; Zhang, S.R.; Erickson, P.J.; Rideout, W.; Vierinen, J. GNSS Observations of Ionospheric Variations During the 21 August 2017 Solar Eclipse. *Geophys. Res. Lett.* **2017**, *44*. [CrossRef]
4. Le, H.; Liu, L.; Yue, X.; Wan, W. The ionospheric responses to the 11 August 1999 solar eclipse: Observations and modeling. *Ann. Geophys. Atmos. Hydrospheres Space Sci.* **2008**, *26*, 107–116. [CrossRef]
5. Chimonas, G.; Hines, C. Atmospheric gravity waves induced by a solar eclipse. *J. Geophys. Res.* **1970**, *75*, 875. [CrossRef]
6. Chimonas, G. Internal gravity-wave motions induced in the Earth's atmosphere by a solar eclipse. *J. Geophys. Res.* **1970**, *75*, 5545–5551. [CrossRef]
7. Fritts, D.C.; Luo, Z. Gravity wave forcing in the middle atmosphere due to reduced ozone heating during a solar eclipse. *J. Geophys. Res. Atmos.* **1993**, *98*, 3011–3021. [CrossRef]
8. Eckermann, S.D.; Broutman, D.; Stollberg, M.T.; Ma, J.; McCormack, J.P.; Hogan, T.F. Atmospheric effects of the total solar eclipse of 4 December 2002 simulated with a high-altitude global model. *J. Geophys. Res. Atmos.* **2007**, *112*. [CrossRef]
9. Davis, M.J.; Da Rosa, A.V. Possible Detection of Atmospheric Gravity Waves generated by the Solar Eclipse. *Nature* **1970**, *226*, 1123. [CrossRef] [PubMed]
10. Cheng, K.; Huang, Y.N.; Chen, S.W. Ionospheric effects of the solar eclipse of 23 September 1987, around the equatorial anomaly crest region. *J. Geophys. Res. Space Phys.* **1992**, *97*, 103–111. [CrossRef]
11. Zerefos, C.; Gerasopoulos, E.; Tsagouri, I.; Psiloglou, B.; Belehaki, A.; Herekakis, T.; Bais, A.; Kazadzis, S.; Eleftheratos, C.; Kalivitis, N.; et al. Evidence of gravity waves into the atmosphere during the March 2006 total solar eclipse. *Atmos. Chem. Phys.* **2007**, *7*, 4943–4951. [CrossRef]
12. Liu, J.; Sun, Y.; Kakinami, Y.; Chen, C.; Lin, C.; Tsai, H. Bow and stern waves triggered by the Moon's shadow boat. *Geophys. Res. Lett.* **2011**, *38*. [CrossRef]
13. Hernández-Pajares, M.; Roma-Dollase, D.; Garcia-Fernàndez, M.; Orus-Perez, R.; García-Rigo, A. Precise ionospheric electron content monitoring from single-frequency GPS receivers. *GPS Solut.* **2018**, *22*, 102. [CrossRef]
14. Zhang, S.R.; Erickson, P.J.; Goncharenko, L.P.; Coster, A.J.; Rideout, W.; Vierinen, J. Ionospheric bow waves and perturbations induced by the 21 August 2017 solar eclipse. *Geophys. Res. Lett.* **2017**, *44*. [CrossRef]
15. Nayak, C.; Yiğit, E. GPS-TEC Observation of Gravity Waves Generated in the Ionosphere during 21 August 2017 Total Solar Eclipse. *J. Geophys. Res. Space Phys.* **2018**, *123*, 725–738. [CrossRef]

16. Sun, Y.Y.; Liu, J.Y.; Lin, C.H.; Lin, C.Y.; Shen, M.H.; Chen, C.H.; Chen, C.H.; Chou, M.Y. Ionospheric bow wave induced by the moon shadow ship over the continent of United States on 21 August 2017. *Geophys. Res. Lett.* **2018**, *45*, 538–544. [CrossRef]
17. Huba, J.; Drob, D. SAMI3 prediction of the impact of the 21 August 2017 total solar eclipse on the ionosphere/plasmasphere system. *Geophys. Res. Lett.* **2017**, *44*, 5928–5935. [CrossRef]
18. McInerney, J.M.; Marsh, D.R.; Liu, H.L.; Solomon, S.C.; Conley, A.J.; Drob, D.P. Simulation of the 21 August 2017 Solar Eclipse Using the Whole Atmosphere Community Climate Model-eXtended. *Geophys. Res. Lett.* **2018**, *45*, 3793–3800. [CrossRef]
19. Wu, C.; Ridley, A.; Goncharenko, L.; Chen, G. GITM-Data Comparisons of the Depletion and Enhancement during the 2017 Solar Eclipse. *Geophys. Res. Lett.* **2018**, *45*, 3319–3327. [CrossRef]
20. Reinisch, B.; Dandenault, P.; Galkin, I.; Hamel, R.; Richards, P. Investigation of the electron density variation during the 21 August 2017 solar eclipse. *Geophys. Res. Lett.* **2018**, *45*, 1253–1261. [CrossRef]
21. Bullett, T.; Mabie, J. Vertical and Oblique Ionosphere Sounding During the 21 August 2017 Solar Eclipse. *Geophys. Res. Lett.* **2018**, *45*, 3690–3697. [CrossRef]
22. Yang, H.; Monte-Moreno, E.; Hernández-Pajares, M. Multi-TID detection and characterization in a dense Global Navigation Satellite System receiver network. *J. Geophys. Res. Space Phys.* **2017**, *122*, 9554–9575. [CrossRef]
23. National Geodetic Survey (NGS). Guidelines for New and Existing Continuously Operating Reference Stations (CORS). 2018. Available online: https://www.ngs.noaa.gov/CORS/ (accessed on 4 October 2018).
24. US Department of Commerce, National Oceanic and Atmospheric Administration (NOAA). Geomagnetic Data. 2017. Available online: https://www.ngdc.noaa.gov/geomag/data.shtml (accessed on 1 March 2018).
25. World Data Center for Geomagnetism, Kyoto. Auroral Electrojet Activity Index. 2018. Available online: http://wdc.kugi.kyoto-u.ac.jp/ae_provisional/201708/index_20170821.html (accessed on 4 October 2018).
26. NOAA National Centers for Environmental Information. National Geophysical Data Center/World Data Service: NCEI/WDS Global Significant Earthquake Database. Available online: https://doi.org/10.7289/V5TD9V7K (accessed on 1 March 2018).
27. NOAA National Centers for Environmental Information. National Geophysical Data Center/World Data Service: NCEI/WDS Global Historical Tsunami Database. Available online: https://doi.org/10.7289/V5PN93H7 (accessed on 1 March 2018).
28. US Department of Commerce, National Oceanic and Atmospheric Administration (NOAA). Solar Data Services: Sun, Solar Activity and Upper Atmosphere Data. 2017. Available online: https://www.ngdc.noaa.gov/stp/solar/solardataservices.html (accessed on 1 March 2018).
29. Hernández-Pajares, M.; Juan, J.; Sanz, J. Medium-scale traveling ionospheric disturbances affecting GPS measurements: Spatial and temporal analysis. *J. Geophys. Res. Space Phys.* **2006**, *111*.[CrossRef]
30. Hernández-Pajares, M.; Juan, J.; Sanz, J.; Aragón-Àngel, A. Propagation of medium scale traveling ionospheric disturbances at different latitudes and solar cycle conditions. *Radio Sci.* **2012**, *47*. [CrossRef]
31. Hernández-Pajares, M.; Juan, J.M.; Sanz, J.; Aragón-Àngel, À.; García-Rigo, A.; Salazar, D.; Escudero, M. The ionosphere: Effects, GPS modeling and the benefits for space geodetic techniques. *J. Geod.* **2011**, *85*, 887–907. [CrossRef]
32. National Aeronautics and Space Administration/Goddard Space Flight Center (NASA/GSFC). International Reference Ionosphere 2012 (IRI-2012) Database. 2012. Available online: https://omniweb.gsfc.nasa.gov/vitmo/iri2012_vitmo.html (accessed on 1 March 2018).
33. Bilitza, D.; Altadill, D.; Zhang, Y.; Mertens, C.; Truhlik, V.; Richards, P.; McKinnell, L.A.; Reinisch, B. The International Reference Ionosphere 2012—A model of international collaboration. *J. Space Weather Space Clim.* **2014**, *4*, A07. [CrossRef]
34. Hastie, T.; Tibshirani, R.; Wainwright, M. *Statistical Learning with Sparsity: The Lasso and Generalizations*; CRC Press: Boca Raton, FL, USA, 2015.
35. Montenbruck, O.; Pfleger, T. *Astronomy on the Personal Computer*; Springer: Berlin/Humberger, Germany, 2013.
36. Andrews, R.W.; Stein, J.; Hansen, C.W.; Riley, D.M. *Introduction to the Open Source PV LIB for Python Photovoltaic System Modeling Package*; Technical Report; Sandia National Lab. (SNL-NM): Albuquerque, NM, USA, 2014.

37. Ionospheric Disturbance Movie, from CORS GNSS Network, for GPS Satellite PRN2, 21 August 2017, 15:00–22:00 UT. Available online: https://www.youtube.com/watch?v=g1IQnLBX6cc (accessed on 8 October 2018).
38. Kazadzis, S.; Bais, A.; Blumthaler, M.; Webb, A.; Kouremeti, N.; Kift, R.; Schallhart, B.; Kazantzidis, A. Effects of total solar eclipse of 29 March 2006 on surface radiation. *Atmos. Chem. Phys.* **2007**, *7*, 5775–5783. [CrossRef]
39. Müller-Wodarg, I.; Aylward, A.; Lockwood, M. Effects of a mid-latitude solar eclipse on the thermosphere and ionosphere—A modelling study. *Geophys. Res. Lett.* **1998**, *25*, 3787–3790. [CrossRef]
40. Ionospheric Disturbance Movie, from CORS GNSS Network, for GPS Satellite PRN12, 21 August 2017, 15:00–22:00 UT. Available online: https://www.youtube.com/watch?v=O8eYn-0jLX4 (accessed on 8 October 2018).
41. Ionospheric Disturbance Movie, from CORS GNSS Network, for all GPS Satellites, 21 August 2017, 15:00–22:00 UT. Available online: https://www.youtube.com/watch?v=zsWsSRD3bcQ (accessed on 8 October 2018).
42. Tsugawa, T.; Saito, A.; Otsuka, Y. A statistical study of large-scale traveling ionospheric disturbances using the GPS network in Japan. *J. Geophys. Res. Space Phys.* **2004**, *109*. [CrossRef]
43. Chimonas, G.; Hines, C. Atmospheric gravity waves launched by auroral currents. *Planet. Space Sci.* **1970**, *18*, 565–582. [CrossRef]
44. Kotake, N.; Otsuka, Y.; Tsugawa, T.; Ogawa, T.; Saito, A. Climatological study of GPS total electron content variations caused by medium-scale traveling ionospheric disturbances. *J. Geophys. Res. Space Phys.* **2006**, *111*. [CrossRef]